Journal of Materials Chemistry A

ROYAL SOCIETY OF CHEMISTRY

PAPER

View Article Online
View Journal | View Issue

Check for updates

Cite this: *J. Mater. Chem. A*, 2025, **13**, 8559

Maximizing thermoelectric performance in SnTe through strategic co-doping, nanostructuring, and topological insights†

Peramaiyan Ganesan, *[a] Chandra Shekar Gantepogu,[a] Sidharth Duraisamy,[a] Phillip Wu,[a] Gwo-Tzong Huang,[a] Muhammad Yusuf Fakhri,[a] Kuei-Hsien Chen,[b] Yang-Yuan Chen[a] and Maw-Kuen Wu*[a]

Enhancing thermoelectric performance through doping is a pivotal strategy, optimizing carrier concentration, reducing energy band separation, and decreasing thermal conductivity. This study delves into the thermoelectric and magneto-transport properties of SnTe single crystals, recognized for their topological insulator characteristics. SnTe's unique electronic states, featuring highly conductive surface states protected by crystal symmetry, significantly boost electrical conductivity while maintaining low thermal conductivity. Consequently, a high thermoelectric figure of merit (*ZT*) of approximately 0.71 is achieved at 873 K along the (111) direction. By fine-tuning carrier concentration and employing nanostructuring techniques, we enhanced the *ZT* of pristine SnTe to 0.75 at 811 K. Additionally, we explored the co-doping effects of Mg, Ag, and Bi on the thermoelectric properties of self-compensated polycrystalline SnTe. Bi-doping effectively reduces carrier concentration, promotes valence band convergence, and lowers thermal conductivity. The co-doping of Bi and Ag induces valence band convergence, further amplified by Mg doping, resulting in high power factors of 20.7 and 22.8 μW cm^{-1} K^{-2} at 872 K in $Sn_{0.94}Ag_{0.03}Bi_{0.06}Te$ and $Sn_{0.86}Ag_{0.03}Mg_{0.08}Bi_{0.06}Te$, respectively. The all-scale hierarchical structure and elemental doping significantly reduce lattice thermal conductivity to ultra-low values of 0.135 and 0.123 W m^{-1} K^{-1} at 873 K in $Sn_{0.94}Ag_{0.03}Bi_{0.06}Te$ and $Sn_{0.86}Ag_{0.03}Mg_{0.08}Bi_{0.06}Te$, respectively. These combined effects yield high *ZT* values of approximately 1.6 and 2.01 at 873 K in $Sn_{0.94}Ag_{0.03}Bi_{0.06}Te$ and $Sn_{0.86}Bi_{0.06}Ag_{0.03}Mg_{0.08}Te$, respectively. Moreover, we conducted de Haas–van Alphen (dHvA) studies to further elucidate the topological surface state properties of SnTe. These investigations enabled us to extract critical parameters such as the cyclotron effective mass, Fermi surface area, and Fermi velocity, offering deeper insights into the electronic structure and enhancing our understanding of the material's unique characteristics. Our findings highlight the significant potential of co-doping and nanostructuring strategies in advancing the thermoelectric performance of SnTe, paving the way for the development of high-efficiency thermoelectric materials.

Received 21st January 2025
Accepted 19th February 2025

DOI: 10.1039/d5ta00582e

rsc.li/materials-a

Introduction

Thermoelectric materials are pivotal in converting heat directly into electricity and *vice versa*, making them highly attractive for power generation, especially amid the current energy crisis. Applications of thermoelectric materials include waste heat recovery from industrial processes, automotive exhaust systems, and power generation in remote sensors and small-scale generators in the mid-temperature range (300–600 K), as well as power generation in space missions (radioisotope thermoelectric generators), high-efficiency waste heat recovery in steel and glass manufacturing, and geothermal energy conversion in the high-temperature range (600–1000 K).[1–7] The efficiency of these materials is determined by the figure of merit (*ZT*), which depends on the Seebeck coefficient (S), electrical conductivity (σ), and total thermal conductivity (κ_{tot}), comprising electronic (κ_e) and lattice (κ_L) components. Optimizing the intertwined parameters of S and σ in the power factor (PF = $S^2\sigma$) and κ_e is challenging, as they rely on carrier transport, necessitating carrier optimization strategies to enhance the power factor. However, increasing carrier concentration typically reduces S, limiting PF values. To address this, strategies such as band sharpening, band convergence, minority carrier blocking, and resonant state doping have been developed to intrinsically improve PF. Conversely, κ_L, which depends solely on phonon transport, can be significantly

[a]*Institute of Physics, Academia Sinica, Taiwan. E-mail: mkwu@phys.sinica.edu.tw; kutty.peram@gmail.com; Fax: +886-2-27896750; Tel: +886-2-27896716*

[b]*Institute of Atomic and Molecular Sciences, Academia Sinica, Taiwan*

† Electronic supplementary information (ESI) available. See DOI: https://doi.org/10.1039/d5ta00582e

reduced through methods like alloying, nanostructuring,[8] and incorporating nano precipitates.[9–19]

Topological insulators (TIs) are promising candidates for thermoelectric applications due to their unique electronic properties. TIs have gapless surface states protected by time-reversal symmetry, which can contribute to high electrical conductivity while maintaining low thermal conductivity. The band inversion in TIs, driven by strong spin–orbit coupling, leads to a warped bulk electronic structure. This warping can enhance thermoelectric performance by reducing the transport mass and effectively increasing valley degeneracy.[1,20–23] Materials like Bi_2Te_3 and Sb_2Te_3 are well-known TIs exhibiting excellent thermoelectric properties.[24–26] These materials have been extensively studied for their potential in thermoelectric devices. Techniques such as alloying, strain engineering, and nanostructuring can be used to optimize the thermoelectric performance of TIs.[27–29] SnTe (tin telluride) stands out due to its unique combination of properties. As a topological crystalline insulator (TCI), SnTe exhibits protected surface states that arise from its crystal symmetry.[30,31] These surface states are robust against certain types of perturbations, making SnTe a promising candidate for applications in quantum computing and spintronics. On the thermoelectric front, SnTe is notable for its potential to convert waste heat into electricity. However, its thermoelectric performance has traditionally been limited by high hole carrier concentration, which results in a low Seebeck coefficient and high thermal conductivity.[32,33] The energy separation between the light and heavy valence bands in SnTe, approximately 0.35 eV,[34] can indeed pose a challenge for achieving a high power factor. This separation can limit the effective mass of the carriers and reduce the density of states near the Fermi level, which in turn affects the Seebeck coefficient and electrical conductivity. Both SnTe and PbTe have a cubic crystal structure at room temperature. However, SnTe undergoes a ferroelectric transition at low temperatures, while PbTe remains an incipient ferroelectric.[35] In terms of band gap, SnTe has a direct band gap of approximately 0.18 eV,[34] whereas PbTe has a slightly larger band gap of about 0.31 eV.[36] Thermoelectrically, PbTe has historically shown superior performance with higher *ZT* values compared to SnTe. This is primarily due to PbTe's lower lattice thermal conductivity and better optimization of carrier concentration.[37] Despite these advantages, the toxicity of lead limits the large-scale application of PbTe, making SnTe a more environmentally friendly alternative. The importance of using low-toxicity elements in thermoelectric materials arises from the need to ensure safety during synthesis, usage, and disposal, mitigating health risks and environmental pollution. To define and categorize low-toxicity elements, we referenced regulatory standards from agencies like the Environmental Protection Agency (EPA) and European Chemicals Agency (ECHA), reviewed scientific literature, and assessed biocompatibility and environmental impact. The selection of Mg, Ag, and Bi as dopants in SnTe was guided by their low toxicity, environmental friendliness, and ability to enhance thermoelectric properties. Recent research has focused on enhancing the thermoelectric properties of SnTe through various methods, including Bi doping and alloying with elements such as Ag, Mn, Zn, Cu, In, Se, Ge, Pd, (Ag, Mg), and CdSe.[32,34,38–51] These strategies help to reduce carrier concentration and adjust the energy offset of the valence bands, thereby improving the thermoelectric figure of merit. Notably, Ag and Mg co-doping in SnTe has demonstrated significant band engineering effects, achieving a figure of merit of approximately 1.55 at 865 K.[47] Additionally, $MnCdTe_2$ alloying in SnTe has shown a remarkable figure of merit of about 1.97 at 900 K.[40] However, the low average *ZT* and the use of toxic elements pose challenges for practical applications. Furthermore, advancements in nanostructuring and the incorporation of nano precipitates have shown promise in reducing lattice thermal conductivity, while emerging techniques like strain engineering and resonant state doping continue to push the boundaries of thermoelectric performance.

Our work thoroughly investigated the thermoelectric properties of both single and polycrystalline SnTe. We extracted key parameters such as the cyclotron effective mass, density of states effective mass, Fermi velocity, quantum mobility, and scattering lifetime from the de Haas–van Alphen quantum oscillations. Our directional studies on SnTe crystals revealed low lattice thermal conductivity along the [111] direction. Additionally, we demonstrated that nanostructuring is an effective approach for SnTe, leading to an enhanced average *ZT* compared to single-crystal SnTe. To further improve the *ZT*, we doped SnTe with Ag, Mg, and Bi, achieving a remarkable *ZT* of about $\approx$2.01 at 873 K in $Sn_{0.86}Ag_{0.03}Mg_{0.08}Bi_{0.06}Te$. Mg tunes carrier concentration, Ag boosts electrical conductivity, and Bi promotes valence band convergence, collectively improving performance while maintaining safety and sustainability.

The X-ray diffraction (XRD) patterns for the pristine and doped SnTe samples, shown in Fig. S1(a),† were obtained using Cu Kα radiation. The diffraction peaks correspond to the cubic rock-salt structure with a space group of *Fm*-3*m*, indicating that the main phase remains SnTe after doping. Significant shifts in diffraction peaks, as seen in Fig. S1(b),† are due to the incorporation of various dopants. To examine phase evolution and impurities, temperature-dependent synchrotron XRD was performed with a wavelength of 0.62 Å for $Sn_{0.94}Ag_{0.03}Bi_{0.06}Te$ and $Sn_{0.86}Ag_{0.03}Mg_{0.08}Bi_{0.06}Te$, as shown in Fig. 1. In Ag and Bi-doped SnTe, both Bi and Ag_5Te_3 precipitates are present. The Bi peak disappears above 523 K, indicating that Bi precipitates dissolve at higher temperatures, while the Ag_5Te_3 peak persists up to 873 K, showing its stability at elevated temperatures. In the $Sn_{0.86}Ag_{0.03}Mg_{0.08}Bi_{0.06}Te$ sample, both MgTe and Ag_5Te_3 precipitates are observed, with the intensity of the MgTe (100) peak increasing up to 573 K and then decreasing, almost disappearing at 923 K. The intensity of the (100) peak of the MgTe precipitate gradually increases, reaching a maximum at 573 K, and then decreases, almost disappearing at 923 K. In samples doped with Ag, Bi, and Mg, the combined effects of these dopants are evident, with shifts in primary peaks reflecting changes in lattice parameters and additional peaks indicating the presence of Ag_5Te_3 and MgTe secondary phases. These structural changes and impurity phases, confirmed by the shifts in diffraction peaks, are crucial for understanding and optimizing the thermoelectric properties of SnTe.

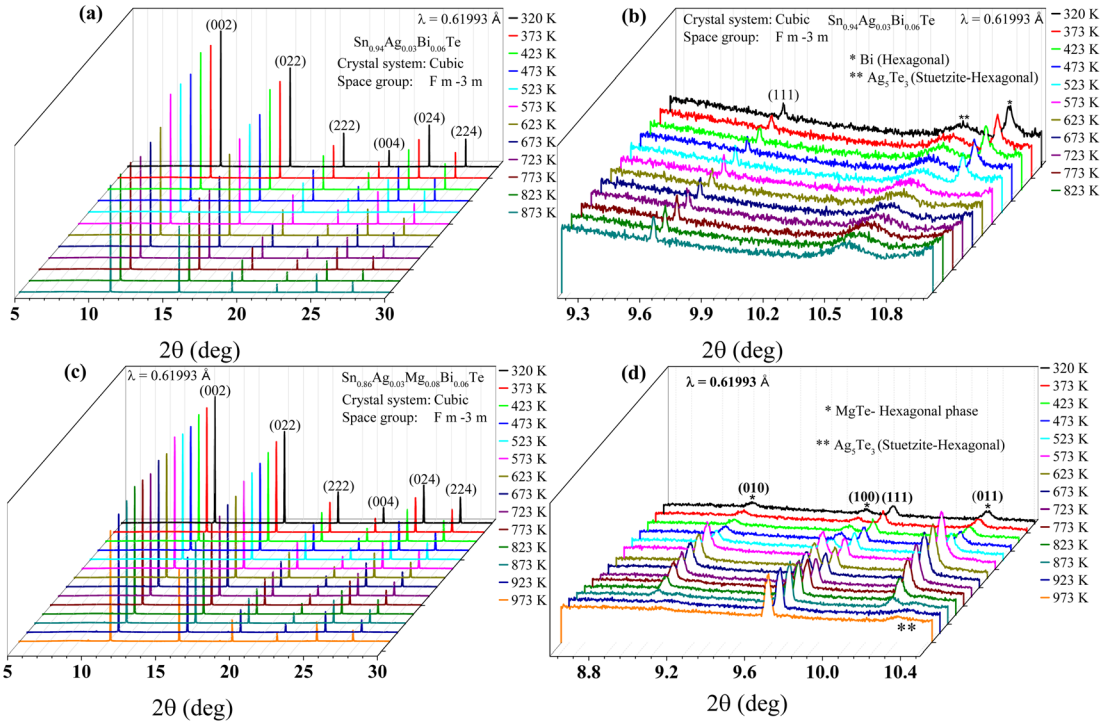

Fig. 1 (a) X-ray diffraction (XRD) patterns of Ag-doped SnTe samples at various temperatures. (b) Enlarged view of the XRD peaks for Bi-doped SnTe samples, indicating the disappearance of Bi peaks above 523 K and the persistence of Ag_5Te_3 peaks up to 873 K. (c) XRD patterns for $Sn_{0.86}Ag_{0.03}Mg_{0.08}Bi_{0.06}Te$ samples, highlighting the presence of MgTe and Ag_5Te_3 precipitates. (d) Detailed peak analysis of the $Sn_{0.86}Ag_{0.03}Mg_{0.08}Bi_{0.06}Te$ samples, showing the temperature-dependent intensity changes of the MgTe (100) peak, which increases up to 573 K and then decreases, almost disappearing at 923 K.

The scanning transmission electron microscopy (STEM) image in Fig. 2(a) reveals MgTe nanoparticles with sizes ranging from 1.3 nm to 10 nm, indicating a uniform distribution within the matrix. Fig. 2(b) highlights the presence of MgTe precipitates, marked by white circles, suggesting successful doping and precipitation. In Fig. 2(c), the yellow rectangle designates the area of the main SnTe matrix where Fast Fourier transform (FFT) analysis was performed, with the inset displaying the FFT pattern, confirming the crystalline nature of the SnTe matrix. Fig. 2(d)–(f) present inverse FFT profiles for the (022), (113), and (111) planes, respectively, confirmed by *d*-spacing measurements. These profiles reveal lattice strain and dislocation defects within the material. The red arrows in these images point to specific features indicating these defects, while the insets show diffraction patterns that further corroborate the presence of these structural anomalies. The presence of MgTe precipitates is further confirmed by Energy Dispersive X-ray Spectroscopy (EDS) measurements, as shown in ESI Fig. S2.† The grain size distribution of $Sn_{0.86}Ag_{0.03}Mg_{0.08}Bi_{0.06}Te$ sample is shown in Fig. S3.† The EDS analysis provides elemental mapping and composition data, verifying the distribution and concentration of MgTe within the sample. These observations suggest that the doping process has introduced significant lattice strain and defects, which could influence the thermoelectric properties of the material.

The thermoelectric properties of single crystal and polycrystalline SnTe were systematically compared to understand the influence of nanostructuring and to elucidate the intrinsic thermoelectric properties of SnTe. The electrical conductivity (σ) as a function of temperature (T) (Fig. 3(a)) shows that both single crystal and polycrystalline SnTe exhibit a decreasing trend with increasing temperature. However, the single crystal SnTe maintains a higher electrical conductivity across the temperature range, attributed to its higher carrier concentration (4.73×10^{20} cm^{-3}) compared to the polycrystalline sample (5.26×10^{19} cm^{-3}). The Seebeck coefficient (S) *versus* temperature (Fig. 3(b)) indicates an increasing trend for single-crystal and polycrystalline SnTe. Interestingly, the polycrystalline SnTe shows a higher Seebeck coefficient than the single crystal SnTe, which can be linked to the differences in carrier concentration and scattering mechanisms. The thermal conductivity (κ) as a function of temperature (Fig. 3(c)) is divided into electronic (κ_e) and lattice (κ_L) components. The polycrystalline SnTe exhibits lower thermal conductivity than the single crystal sample across the temperature range. This is likely due to increased phonon scattering at grain boundaries and defects in the polycrystalline structure. Additionally, the thermoelectric properties were studied along the [010] and [111] crystallographic directions, revealing that the [111] direction shows lower thermal conductivity than the [010] direction, which is consistent with reported phonon transport studies on SnTe. These studies highlight the strong anharmonicity in SnTe's phonon spectra, influenced by its resonant bonding and crystal structure, leading to different phonon lifetimes and

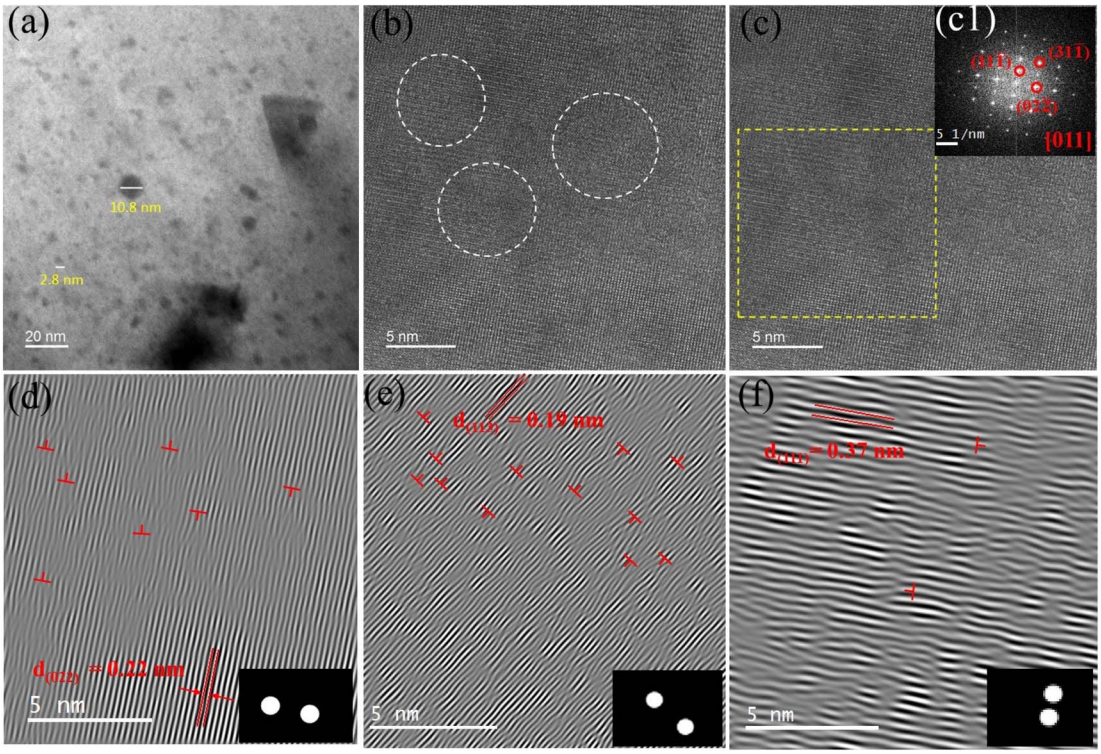

Fig. 2 Transmission electron microscopy (TEM) studies on $Sn_{0.86}Ag_{0.03}Mg_{0.08}Bi_{0.06}Te$. The STEM image (a) shows MgTe nanoparticles ranging from 1.3 nm to 10 nm. The TEM image (b) highlights MgTe precipitates with white circles. In (c), the yellow rectangle indicates the area for FFT analysis, with the inset showing the FFT pattern. Images (d)–(f) display IFFT profiles, revealing lattice strain and dislocation defects, with red arrows pointing to these features. The insets in these images show diffraction patterns.

scattering mechanisms along various crystallographic directions. The local off-centering of Sn^{2+} ions along the ⟨111⟩ direction creates significant lattice distortions and scattering centers, reducing thermal conductivity in this direction. In contrast, the ⟨010⟩ direction experiences fewer distortions and less scattering, resulting in higher thermal conductivity.[35,52–54] The polycrystalline SnTe shows lower κ_L of 0.47 W m^{-1} K^{-1} at 500 K, but an increased trend at higher temperatures due to bipolar contribution. While the complete phase transition to a rhombohedral structure (full ferroelectric phase) occurs below 114 K (Fig.S6(a)†), these local ferroelectric domains persist in the cubic phase above 114 K, all the way to high temperatures. Studies have confirmed these local domains at room temperature,[52] significantly influencing SnTe's thermal and electrical properties. The interplay between cubic and ferroelectric phases could introduce phonon Berry curvature, resulting in phenomena like the nonlinear phonon Hall effect, further modulating heat transport. This transition at 112 K in the MT (magnetization *vs.* temperature) curve for the polycrystalline sample aligns well with our resistivity findings (Fig.S6(b)†). It indicates that the phase transition is indeed affecting the magnetic properties. The fact that it's less pronounced in the single crystal but still visible suggests that the structural transition impacts both types but is more accentuated in polycrystalline due to increased scattering at grain boundaries and defects. Such observations highlight the intricate interplay between structural phase transitions and magnetic properties, which can be pivotal for understanding the material's full range of behaviors and potential applications. By ruling out carrier concentration dependent phase transition speculation,[55] our findings provide a clearer focus on the intrinsic structural influences at play. The figure of merit (*ZT*) *versus* temperature (Fig. 3(d)) demonstrates that *ZT* values increase with temperature for both single crystal and polycrystalline SnTe. However, the polycrystalline SnTe achieves higher *ZT* values compared to the single crystal SnTe, indicating superior thermoelectric performance. The average *ZT* of polycrystalline SnTe is about 0.29 for the temperature range of 300 to 811 K and 0.34 for 500 to 811 K.

The weighted mobility (μ_W) *versus* *T* (Fig. 3(e)) shows a decreasing trend with increasing log(*T*) for both types of SnTe. The single crystal SnTe maintains higher mobility, which can be attributed to fewer grain boundaries and defects, leading to less scattering of charge carriers. The temperature dependence of the weighted mobility provides insights into the scattering mechanisms at play. The temperature dependence of the weighted mobility reveals that for single crystal SnTe, the mobility follows a T^{-2} dependence up to the mid-temperature range, indicating significant phonon-boundary scattering and transitions to a T^{-1} dependence at high temperatures, where phonon–phonon Umklapp scattering becomes dominant. In contrast, polycrystalline SnTe exhibits a $T^{-1.4}$ dependence up to the mid-temperature range, suggesting boundary and defect scattering, and a $T^{-2.05}$ dependence at high temperatures, likely

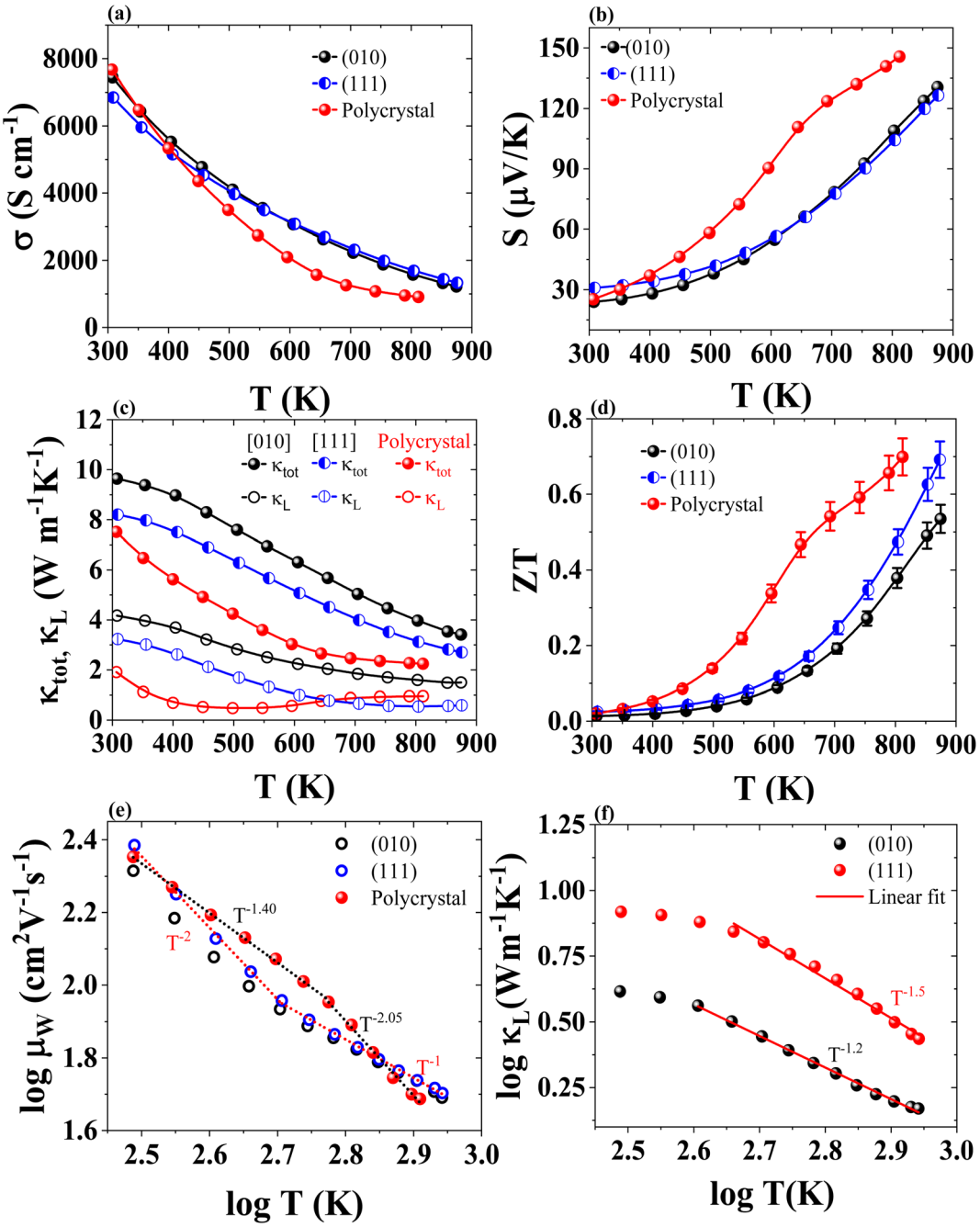

Fig. 3 Temperature-dependent electrical and thermal properties of SnTe single crystal and polycrystalline samples. (a) Electrical conductivity (σ). (b) Seebeck coefficient (S). (c) Thermal conductivity, including both total (κ_{tot}) and lattice (κ_L) components, for the [010] and [111] directions in single crystal and polycrystalline samples. (d) Figure of merit (ZT). (e) Weighted mobility *versus* temperature plot, showing different temperature dependencies and scattering mechanisms. (f) Log κ_L *versus* log T plot for the [010] and [111] directions, where the [010] direction shows a $T^{-1.2}$ dependence and the [111] direction shows a $T^{-1.5}$ dependence.

due to grain boundary and defect scattering. The log(κ_L) *versus* log(T) plot (Fig. 3(f)) presents the lattice thermal conductivity as a function of temperature on a logarithmic scale for a single crystal. The linear fit applied to the data indicates that single-crystal SnTe has lower lattice thermal conductivity along the (111) direction than the (010) direction, confirming the anisotropic phonon dispersion and further supporting directional-dependent scattering mechanisms.

In this study, we investigated the de Haas–van Alphen (dHvA) oscillations in SnTe single crystals along the (010) crystallographic direction, as shown in Fig. 4(a). The magnetization measurements were conducted at low temperatures, and the data were analyzed using the Lifshitz–Kosevich (L–K) fit to extract key electronic properties. The L–K formula accounts for multiple valleys, increasing the effective mass by providing more available states for carriers.[56] The cyclotron effective mass

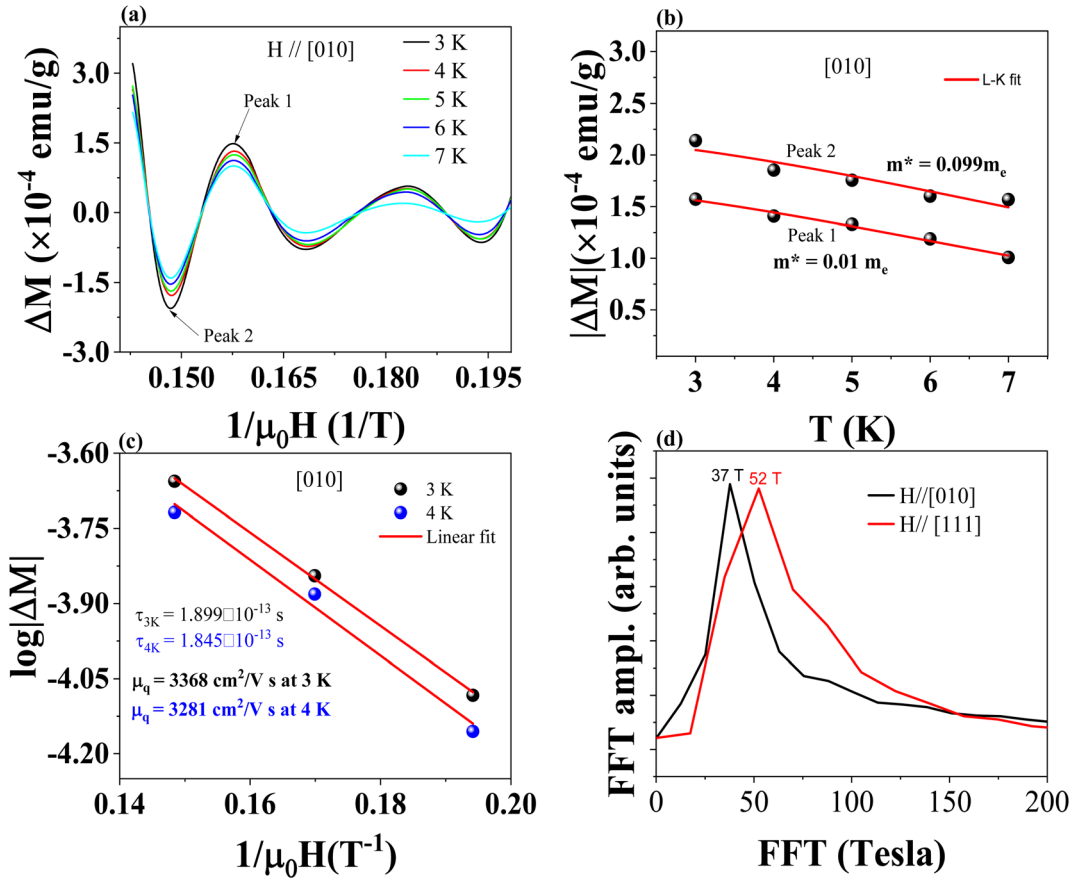

Fig. 4 (a) dHvA oscillations as a function of the inverse magnetic field (1/*H*) for different temperatures (3, 4, 5, 6, and 7 K), showing quantum oscillations indicative of the Fermi surface properties. (b) Peak oscillatory magnetization as a function of temperature, with the red curve representing the Lifshitz–Kosevich (L–K) fit used to calculate the cyclotron effective mass. Peak 1 and Peak 2 indicate the positions of peak oscillatory magnetization at different fields. (c) Peak oscillatory magnetization as a function of the inverse magnetic field, highlighting the periodic nature of the dHvA oscillations. The linear fit is used to estimate the Dingle temperature and scattering lifetime. (d) FFT amplitude *versus* FFT frequency, showing the frequency components of the oscillations, which correspond to extremal cross-sectional areas of the Fermi surface. The FFT frequencies for the (010) and (111) directions are consistent with reported data.

(m_c^*) of the charge carriers in single crystal SnTe was determined to be 0.09 m_e (Fig. 4(b)) from de Haas–van Alphen (dHvA) measurements at 3 K, indicating that the charge carriers are light and contribute to higher mobility. Measurements along the [010] and [111] crystallographic directions yielded consistent values for the cyclotron effective mass, confirming the isotropic nature of the band structure in SnTe. Consequently, (m_c^*) can be reliably equated to (m_d^*) in this material. However, different thermal conductivities observed along these directions indicate anisotropic lattice dynamics. For pristine polycrystalline SnTe, the density of states (DOS) effective mass (m_d^*) was estimated to be 0.173 m_e using the Snyder[57,58] formula at 300 K. This difference highlights the impact of crystallographic structure and temperature on the effective mass. The consistency between the effective masses obtained using different methods and conditions indicates a robust electronic structure across different modelling approaches.

The scattering lifetime was found to be approximately 1.899×10^{-23} s at 3 K and 1.845×10^{-23} s at 4 K (Fig. 4(c)). The quantum mobility was calculated to be 3368 $cm^2\ V^{-1}\ s^{-1}$ at 3 K and 3281 $cm^2\ V^{-1}\ s^{-1}$ at 4 K, confirming the efficient transport properties of the charge carriers in SnTe. This is in close agreement with the Hall mobility of about 3221 $cm^2\ V^{-1}\ s^{-1}$ at 3 K. Fig. 4(d) shows the Fast Fourier Transform (FFT) analysis of the dHvA oscillations revealed frequencies of 37 T for the (010) direction and 52 T for the (111) direction, corresponding to Fermi surface areas of 3.528×10^{-3} $Å^{-2}$ and 4.958×10^{-3} $Å^{-2}$, respectively. The Fermi vectors were found to be 0.033 $Å^{-1}$ for the (010) direction and 0.039 $Å^{-1}$ for the (111) direction, with corresponding velocities of 4.31×10^5 m s^{-1} and 5.11×10^5 m s^{-1}. These values suggest that the charge carriers experience relatively infrequent scattering events, indicative of high crystal quality and low impurity levels. The extracted parameters align with those reported in the literature,[31] indicating the presence of a nontrivial Berry phase and confirming the existence of topological surface states in SnTe,[30] as supported by studies such as the one by Dybko *et al.*[31] Notably, we observed that the DOS effective mass for single crystal SnTe is significantly higher (0.648 m_e) than polycrystalline SnTe (0.174 m_e) at 300 K. Despite an order of magnitude difference in carrier concentration, the Seebeck coefficient remains relatively stable, measuring 24 μV K^{-1} for single crystal and 25 μV K^{-1} for

polycrystalline SnTe at 300 K. This stability suggests that the intrinsic electronic properties are optimized through the material's unique characteristics. The presence of topological surface states and a Dirac cone in single crystal SnTe, which introduces linear band dispersion, likely contributes to the higher DOS effective mass. These topological surface states enhance the electronic properties by providing additional electronic pathways, which are more pronounced in the single crystal form due to the absence of grain boundaries and defects. Given that the Seebeck coefficient remains consistent across both forms, efforts should be focused on minimizing lattice thermal conductivity to improve thermoelectric performance. These observations collectively suggest that the nanostructuring process has introduced significant lattice strain and defects, which play a crucial role in influencing the thermoelectric properties of SnTe along with topological surface states. Interestingly, polycrystalline SnTe demonstrates better *ZT* values than single-crystal SnTe. However, the single crystal SnTe still shows comparable *ZT*, benefiting from higher carrier concentration, better crystallinity, and lower lattice thermal conductivity. This highlights the robust thermoelectric performance of SnTe across different structural forms.

Fig. 5 illustrates the thermoelectric properties of polycrystalline $Sn_{1.03}Te$ with various dopants. The electrical conductivity (σ) of all samples decreases with temperature, indicating a degenerate semiconductor character, as shown in Fig. 5(a). Self-compensated SnTe exhibits high electrical conductivity of approximately 7670 S cm^{-1}, with a carrier mobility of around 908 cm^2 V^{-1} s^{-1}. Ag-doping enhances conductivity at high temperatures by increasing the carrier concentration from 5.27 × 10^{19} cm^{-3} to 1.89 × 10^{20} cm^{-3}. In contrast, the conductivity of $Sn_{0.95}Mg_{0.08}Te$ decreases to 2347 S cm^{-1}, though it maintains decent σ at high temperatures. Combined doping with Ag (3 atm%), Bi (6 atm%), and Mg (8 atm%) in $Sn_{1.03}Te$ further reduces conductivity to 1703 S cm^{-1} due to lower carrier concentration and enhanced carrier scattering. Fig. 5(b) shows that Mg doping results in a higher Seebeck coefficient than singly and doubly doped SnTe. Combined doping with Ag, Mg, and Bi balances these effects, resulting in high Seebeck coefficients. This combination achieves a high power factor of approximately 22.8 μW cm^{-1} K^{-2} at 872 K, as shown in Fig. 5(c). Fig. 5(d) illustrates the variation in carrier concentration (n_h) and mobility (μ_h) for different dopings. Excess Sn significantly reduces the hole concentration while maintaining high carrier mobility. Notably, in Mg-doped SnTe, n_h is significantly decreased to 4.80 × 10^{19} cm^{-3} with mobility of 293 cm^2 V^{-1} s^{-1}. Since Mg is likely to be 2+ like Sn, it mitigates the formation of Sn vacancies, which helps maintain a lower carrier concentration and enhances the Seebeck coefficient. In triply doped $Sn_{0.86}Ag_{0.03}Mg_{0.08}Bi_{0.06}Te$, the carrier concentration slightly increases to 9.9 × 10^{19} cm^{-3}, while maintaining a mobility of 112.07 cm^2 V^{-1} s^{-1}.

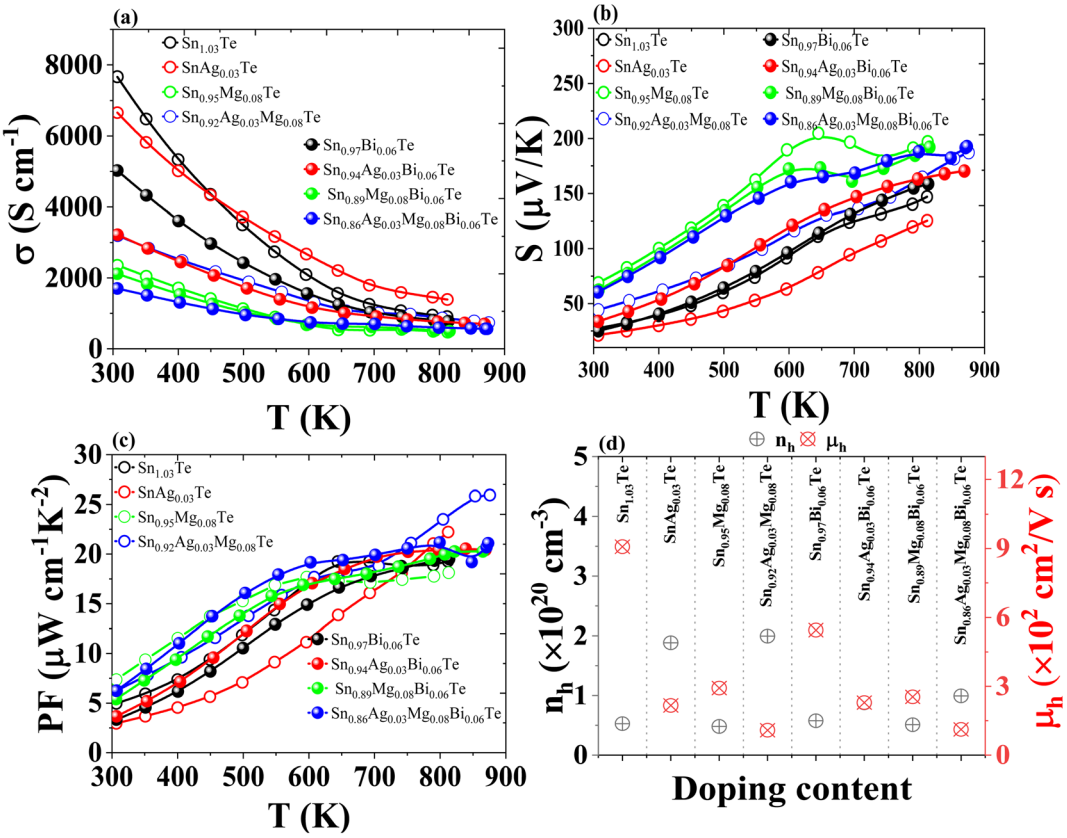

Fig. 5 Temperature-dependent thermoelectric properties of polycrystalline and doped SnTe samples. (a) Electrical conductivity (σ). (b) Seebeck coefficient (S). (c) Power factor (PF). (d) Carrier concentration (n_h) and mobility (μ_h) vary with doping.

Our research has demonstrated an enhanced power factor in doped SnTe, primarily due to an increased Seebeck coefficient. However, the precise mechanisms behind this improvement were not fully understood. To gain deeper insights, we conducted a detailed analysis using Pisarenko plots and density of states (DOS) effective mass calculations. We utilized the Pisarenko plot methodology reported by Riddhimoy Pathak *et al.*,[47] which accounts for contributions from both light and heavy hole valence bands. The Pisarenko curve plots the room temperature Seebeck coefficients of SnTe and its doped variants against carrier concentration, considering contributions from both light and heavy hole valence bands with varying energy gaps, as shown in Fig. 6(a). The energy difference between the light and heavy bands is approximately 0.35 eV.[47] For pristine SnTe, the Seebeck value follows the single-band contribution. Bi-doped SnTe matches the curve for a 0.27 eV energy difference, while Ag and Bi co-doped SnTe shows a Seebeck value well above the single band contribution. Mg doping significantly decreases the energy difference, aligning closely with 0.10 eV. The triply-doped Ag, Mg, and Bi in SnTe also aligns closely with 0.10 eV, better than singly and doubly co-doped SnTe. Additionally, Bi doping, whether with Mg, Ag, or both, subtly decreases the energy difference, contributing to the overall enhancement of thermoelectric properties.

The DOS effective mass (m_d^*) was calculated using the expression reported by Snyder *et al.*, as shown in Fig. 6(b). For pristine SnTe ($Sn_{1.03}Te$), the DOS effective mass is 0.173 m_e. When doped with Ag, the DOS effective mass increases to 0.319 m_e, and with Mg doping alone, it further increases to 0.353 m_e. Bi-doping results in a lower DOS effective mass of 0.167 m_e. Co-doping with Ag and Bi increases the DOS effective mass to 0.325 m_e, while Mg and Bi co-doping results in a DOS effective mass of 0.327 m_e. Ag and Mg co-doping significantly increases the DOS effective mass to 0.605 m_e, and triply doping with Ag, Mg, and Bi further increases it to 0.627 m_e. Importantly, the carrier concentration of all samples is in the range of 4.8 to 9.9 $\times 10^{19}$ cm^{-3}, which is not significantly different from pristine $Sn_{1.03}Te$. This consistency in carrier concentration allows us to attribute the observed changes in band structure primarily to the doping effects. Mg doping significantly decreases the energy difference between the lighter and heavier bands, thereby increasing the DOS effective mass. This is consistent with the estimated effective mass values. The combined doping strategies of Ag, Mg, and Bi further enhance the thermoelectric properties by optimizing the band structure. These findings highlight the importance of doping strategies in tuning the electronic properties of SnTe for improved thermoelectric performance.

The thermal conductivity of SnTe and its doped variants with Ag, Mg, and Bi is shown in Fig. 7. Pristine $Sn_{1.03}Te$ shows a room temperature thermal conductivity of about 7.95 W m^{-1} K^{-1}, which is lower than reported values. It decreases significantly with temperature up to 650 K and then starts to increase due to bipolar contribution (Fig. 7(a)). Ag doping slightly increases the total thermal conductivity due to enhanced electronic thermal conductivity. Mg doping results in a very low total thermal conductivity of about 2.48 W m^{-1} K^{-1}, with an upward trend above 600 K and a decline after 700 K. Bi doping alone shows a remarkable reduction in κ_{tot} without bipolar contribution, attributed to reduced electronic thermal conductivity, point defects, and Bi precipitates. Co-doping with Ag and Bi significantly reduces thermal conductivity, particularly at high temperatures, due to point defects, large mass and strain field fluctuations, and Bi and Ag_5Te_3 precipitates. Ag_5Te_3 is known for its intrinsically low thermal conductivity, primarily due to its complex crystal structure and low sound velocity.[59] Mg and Bi co-doping results in an almost flat thermal conductivity trend from 300 K to 811 K with a suppressed bipolar contribution. The combination of Ag, Mg, and Bi doping reduces κ_{tot} to 0.91 W m^{-1} K^{-1} at 873 K, with κ_L as low as 0.123 W m^{-1} K^{-1}, as shown in Fig. 7(b), this reduction is comparable to the values obtained in $(Sn_{0.985}In_{0.015}Te)_{0.90}(AgCl)_{0.10}$, as shown in Fig. 7(b) of the referenced study.[60] It is clear that MgTe, Sn, Bi, and Ag_5Te_3 precipitates contribute to reducing κ_L.

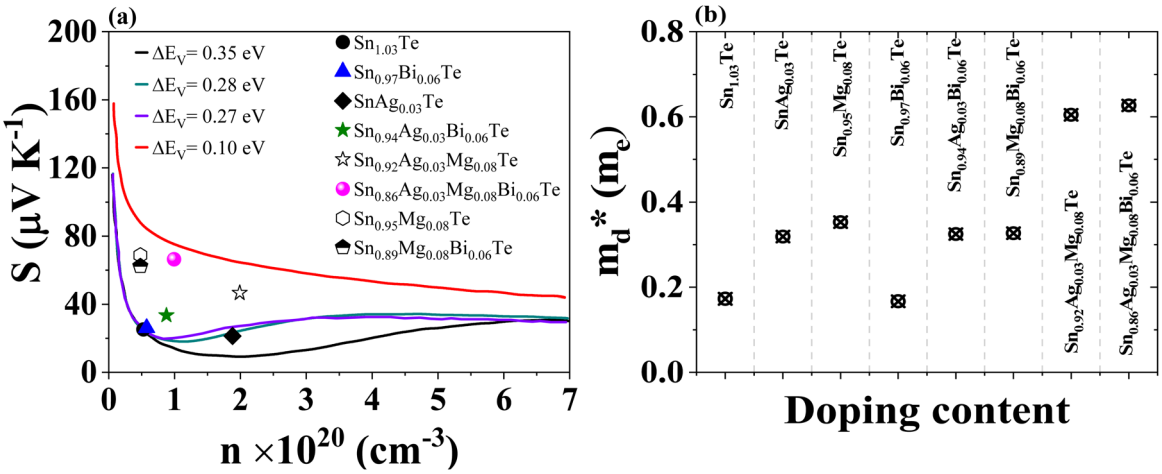

Fig. 6 (a) Pisarenko plot showing the Seebeck coefficient *versus* carrier concentration for SnTe, considering contributions from both light and heavy hole valence bands with varying energy gaps ($\Delta E \approx$ 0.35 eV, 0.28 eV, 0.27 eV and 0.10 eV).[47] (b) Density of states effective mass for pristine and doped SnTe samples. Ag, Mg, and Bi doping increase the effective mass, with Mg doping alone showing a significant increase.

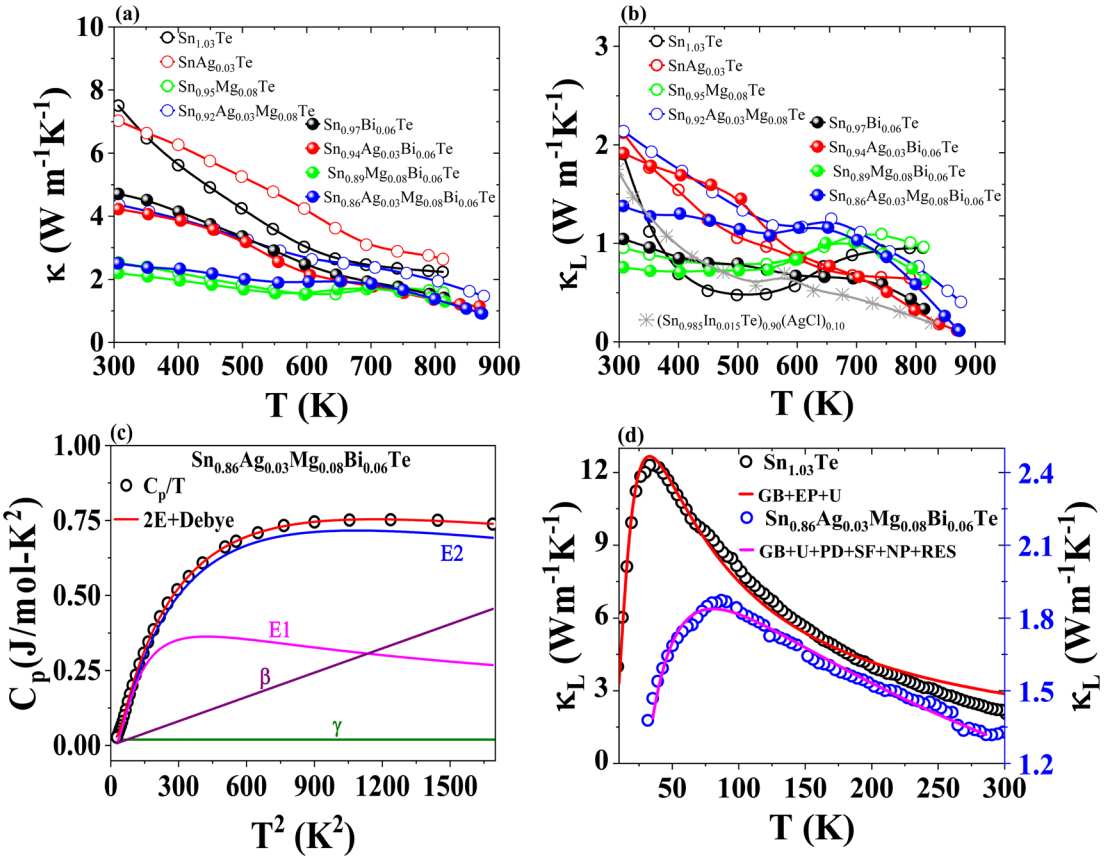

Fig. 7 (a) Total thermal conductivity (κ_{tot}) of pristine $Sn_{1.03}Te$ and its doped variants with Ag, Mg, and Bi as a function of temperature. (b) Lattice thermal conductivity (κ_L). κ_L of $(Sn_{0.985}In_{0.015}Te)_{0.90}(AgCl)_{0.10}$ is included for comparison. (c) Lattice thermal conductivity of $Sn_{1.03}Te$ and $Sn_{0.86}Ag_{0.03}Mg_{0.08}Bi_{0.06}Te$ fitted with the Debye–Callaway model, showing contributions from various phonon scattering mechanisms such as Umklapp process (U), boundary scattering (B), point-defect scattering (PD), nanoparticle scattering (NP), stacking faults scattering (SF), and resonant energy scattering (RES). (d) Specific heat capacity (C_p) divided by temperature (C_p/T) *versus* the square of temperature (T^2) for $Sn_{0.86}Ag_{0.03}Mg_{0.08}Bi_{0.06}Te$, fitted with the Debye–Einstein model, indicating the presence of one Debye mode and two Einstein modes.

To further understand such ultralow κ_L, we conducted Debye–Callaway[61,62] and Debye–Einstein model[63] analyses. The Debye–Einstein model was specifically chosen for C_p analysis because it effectively captures the contributions of both acoustic and optical phonon modes, which are crucial for understanding the phonon scattering mechanisms in doped SnTe. Optical phonon modes introduce additional phonon scattering and impede the normal transport of acoustic phonons with similar frequencies, resulting in low κ_L. The temperature-dependent C_p data is fitted well with one Debye mode and two Einstein modes (Fig. 7(c)). From the fitted parameters (given in Table S1†), the Debye temperature (θ_D) is estimated to be 126.6 K. We extended the thermal conductivity analysis using average sound velocity (1658 m s^{-1})[47] and θ_D to understand the influence of different phonon scattering mechanisms on the ultralow κ_L of the (Ag, Mg, and Bi) co-doped SnTe. The measured κ_L below 300 K is fitted based on the Debye–Callaway model, as shown in Fig. 7(d), by considering phonon scattering mechanisms such as the Umklapp process (U), boundary scattering (B), point-defect scattering related to mass and strain field fluctuations (PD), nanoparticle scattering (NP), stacking faults scattering (SF), and resonant scattering (RES). The model is selected due to its comprehensive approach to phonon transport, providing a robust framework for analyzing complex materials. However, it has limitations arising from simplifying assumptions, such as the phonon dispersion relation, which may not fully capture the material's complexity. Additionally, the model's accuracy heavily depends on precisely determined scattering parameters, with minor inaccuracies potentially leading to significant deviations. Discrepancies between experimental and modelled values, especially at low temperatures, may occur due to these assumptions, inhomogeneities in doping concentration and distribution, and experimental measurement errors. The phonon mean free path of SnTe is about 10 nm.[64] In $Sn_{0.86}Ag_{0.03}Mg_{0.08}Bi_{0.06}Te$, MgTe nanoprecipitates with sizes varying from 1.3 nm to 10 nm are effective in scattering phonons and thus reducing κ_L. Additionally, the presence of Ag_5Te_3 precipitates, a low thermal conductivity material, further contributes to the reduction in thermal conductivity. The Debye–Einstein model analysis revealed two Einstein modes and one Debye mode, indicating the presence of optical phonon modes that introduce additional phonon scattering. These combined effects of nanoprecipitates, precipitates of low thermal conductivity materials, and the presence of optical phonon

modes result in the observed ultralow κ_L in our doped SnTe samples. These findings provide a comprehensive understanding of the factors contributing to reduced thermal conductivity, which is crucial for optimizing the thermoelectric performance of SnTe.

Fig. 8(a) shows the thermoelectric figure of merit (ZT) for SnTe and its doped variants (Ag, Mg, and Bi) as a function of temperature, highlighting the enhanced performance due to doping. Fig. 8(b) compares the average ZT values of these doped SnTe compounds over two temperature ranges (300–870 K and 500–870 K) with other reported SnTe materials, demonstrating the superior thermoelectric efficiency of the doped SnTe variants. This indicates that doping SnTe with these elements significantly improves its thermoelectric properties, making it a promising material for thermoelectric applications. Notably, $Sn_{0.92}Ag_{0.03}Mg_{0.08}Te$ shows a ZT of about $\approx$1.55 at 865 K, consistent with reported data. Pristine nanostructured SnTe exhibits better average ZT than other reported values. Ag and Bi doping enhances ZT, similar to Ag and Mg doping, but with less impressive average ZT. Mg doping significantly increases average ZT, achieving a peak ZT of about $\approx$2 at 873 K and an average ZT of $\approx$0.66 between 300–873 K. We fairly reproduced the thermoelectric data as shown in Fig. S4.† Fig. S5† shows the thermogravimetric curve of $Sn_{0.86}Ag_{0.03}Mg_{0.08}Bi_{0.06}Te$. The 5% of weight loss above 823 K to 873 K does not show any significant changes in thermoelectric transport data.

To understand the doping effects on the topological characteristics, we performed a resistivity analysis of pristine and doped polycrystalline SnTe, revealing significant insights into their topological characteristics. The resistivity model used in this analysis is $\rho(T) = \rho_0 + A\cdot\sqrt{T} - B\ln(T)$, where ρ_0 represents the residual resistivity, A corresponds to weak antilocalization (WAL) effects, and B corresponds to weak localization (WL) or electron–electron interactions (EEI) effects. This model is based on the weak antilocalization theory described in detail by Hikami, Larkin, and Nagaoka (1980).[66,67] Pristine SnTe exhibits high intrinsic conductivity ($\rho_0 = 7.39 \times 10^{-7}$ Ω m), strong weak antilocalization (WAL) effects ($A = 3 \times 10^{-7}$ Ω m), and pronounced weak localization (WL) effects ($B = -5.68 \times 10^{-7}$ Ω m), indicating robust topological surface states and quantum interference effects typical of topological insulators. Interestingly, pristine SnTe shows a metal–insulator (M–I) transition at approximately 12.5 K, indicating the presence of complex interactions and possible disorder even in the pristine sample, as shown in Fig. S7.† In contrast, doped SnTe shows increased residual resistivity ($\rho_0 = 4.23 \times 10^{-6}$ Ω m) due to introduced disorder and impurities but retains weak antilocalization effects ($A = 1.52 \times 10^{-7}$ Ω m), suggesting the preservation of some topological characteristics. The weaker WL effects ($B = -2.29 \times 10^{-7}$ Ω m) and the observation of an M–I transition at approximately 10 K in doped SnTe highlight the significant impact of disorder introduced by doping, disrupting conductive pathways and altering electronic behavior.

Our comprehensive study reveals significant enhancements in the thermoelectric performance of SnTe through strategic doping and nanostructuring, capitalizing on its topological insulator properties. The highly conductive surface states of SnTe, protected by crystal symmetry, contribute to high electrical conductivity while maintaining low thermal conductivity. Doping with Mg, Ag, and Bi optimizes carrier concentration, induces valence band convergence, and reduces thermal conductivity through solid solution point defects and nanoprecipitates. Mg plays a crucial role in band engineering, increasing the density of states (DOS) effective mass, and reducing thermal conductivity, particularly at low temperatures. However, its impact on thermal conductivity is less significant at high temperatures. In contrast, Bi doping effectively reduces thermal conductivity across a broader temperature range, while also optimizing carrier concentration, reducing the energy difference between valence bands, and introducing lattice strain. Ag enhances the effective mass (m_d^*), and when combined with Mg, it further increases the DOS effective mass more effectively than either element alone. HRTEM and synchrotron X-ray diffraction measurements support the presence of MgTe nanoprecipitates and Ag_5Te_3 and MgTe secondary phases. These synergistic effects result in high power factors

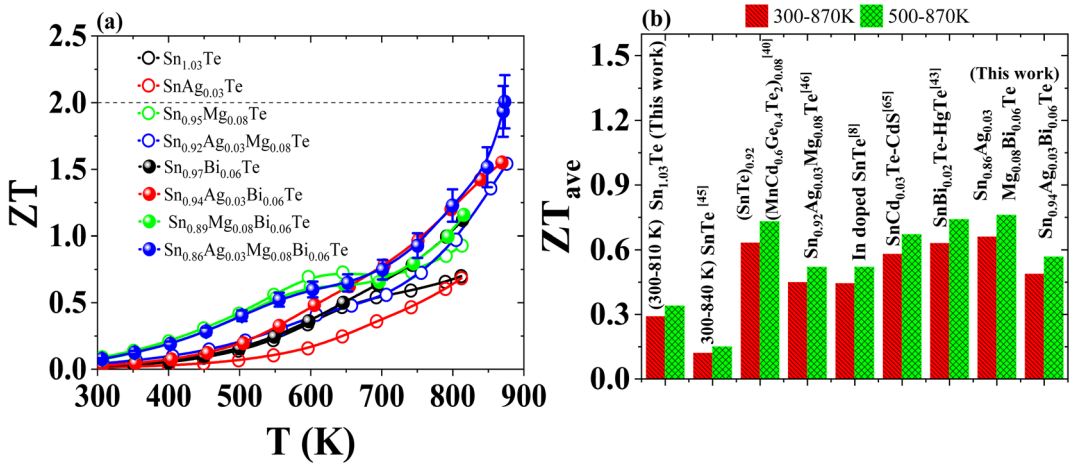

Fig. 8 Thermoelectric performance comparison of doped SnTe compounds: (a) ZT values as a function of temperature for various doped SnTe variants,[65] and (b) average ZT values over different temperature ranges compared with other reported materials.

and substantial improvements in the thermoelectric figure of merit (ZT), with peak values reaching approximately ≈ 2 at 873 K. Additionally, de Haas–van Alphen (dHvA) studies provided deeper insights into the topological surface state properties of SnTe, further elucidating its unique electronic structure. Our dHvA oscillation studies confirm the isotropic electronic band structure, whereas thermal transport studies reveal the anisotropic phonon transport. These findings underscore the potential of co-doping and nanostructuring strategies in developing high-efficiency thermoelectric materials, paving the way for future advancements in thermoelectric technology.

Data availability

The data that support the findings of this study are available from the corresponding author, upon reasonable request. The data include [brief description of data types, such as raw data, processed data, ESI,† *etc.*]. Due to [any reasons for restrictions, such as privacy or ethical concerns], certain data are not publicly available but can be shared under specific conditions.

Author contributions

P. G. designed the project, prepared the samples, and P. G. and S. D. performed thermoelectric transport measurements. C. G. conducted the powder X-ray diffraction and magnetization measurements. P. G. and S. D. conducted TEM experiments and analyzed magnetization data. M. Y. F. performed the diffusivity measurement. P. W. supervised, reviewed, and edited the manuscript. G. T. H. performed the synchrotron X-ray diffraction measurements. Y. Y. conceptualized the project and provided material processing facilities. K. H. C. provided the facility for the diffusivity measurement. P. G. contributed to data analysis, writing the original draft, review, and editing. M. K. contributed to conceptualization, investigation, resources, supervision, funding acquisition, review, and editing.

Conflicts of interest

The authors declare no competing interests.

Acknowledgements

The authors thank Taiwan's Ministry of Science and Technology (MOST) for the research startup grant (MOST110-2112-M-001-063) and Center for Sustainability Science, Academia Sinica [project AS-SS-112–01]. Phillip M. Wu acknowledges the support from the National Science and Technology Council of Taiwan grant number NSTC 113-2112-M-001-022-MY2. We extend our sincere gratitude to the Core Facility Center of National Cheng Kung University for the FIB facility and the Institute of Physics, Academia Sinica, for providing the X-ray diffraction measurement facilities. Our thanks also go to Dr Sankar Raman for the crystal growth facilities and Dr Ou Min-Nan for the Lau-X-ray diffraction facility.

References

1 I. Petsagkourakis, K. Tybrandt, X. Crispin, I. Ohkubo, N. Satoh and T. Mori, *Sci. Technol. Adv. Mater.*, 2018, **19**, 836–862.
2 B. Ma, H. Ren, F. Zhang, Z. Peng, H. He, M. Cui, Z. Ge, B. Li, W. Wu, P. Liang, Y. Xiao, X. Chao, Z. Yang and D. Wu, *Small*, 2023, **19**, 2206439.
3 K. Biswas, Z. Ren, Y. Grin, K. H. Lee, T. Mori and L. Chen, *Appl. Phys. Lett.*, 2022, **121**, 070401.
4 Y. Pei, X. Shi, A. LaLonde, H. Wang, L. Chen and G. J. Snyder, *Nature*, 2011, **473**, 66–69.
5 K. Song, A. N. M. Tanvir, M. O. Bappy and Y. Zhang, *Small Sci.*, 2024, 2300359.
6 J. P. Heremans, V. Jovovic, E. S. Toberer, A. Saramat, K. Kurosaki, A. Charoenphakdee, S. Yamanaka and G. J. Snyder, *Science*, 2008, **321**, 554–557.
7 Y. Xiao, D. Wang, B. Qin, J. Wang, G. Wang and L.-D. Zhao, *J. Am. Chem. Soc.*, 2018, **140**, 13097–13102.
8 Q. Zhang, B. Liao, Y. Lan, K. Lukas, W. Liu, K. Esfarjani, C. Opeil, D. Broido, G. Chen and Z. Ren, *Proc. Natl. Acad. Sci. U. S. A.*, 2013, **110**, 13261–13266.
9 Q. Zhang, B. Liao, Y. Lan, K. Lukas, W. Liu, K. Esfarjani, C. Opeil, D. Broido, G. Chen and Z. Ren, *Proc. Natl. Acad. Sci. U. S. A.*, 2013, **110**, 13261–13266.
10 D. Sarkar, T. Ghosh, A. Banik, S. Roychowdhury, D. Sanyal and K. Biswas, *Angew. Chem., Int. Ed.*, 2020, **59**, 11115–11122.
11 R. Pathak, D. Sarkar and K. Biswas, *Angew. Chem., Int. Ed.*, 2021, **60**, 17686–17692.
12 Z. Liu, W. Gao, H. Oshima, K. Nagase, C.-H. Lee and T. Mori, *Nat. Commun.*, 2022, **13**, 1120.
13 Y. Xiao, D. Wang, Y. Zhang, C. Chen, S. Zhang, K. Wang, G. Wang, S. J. Pennycook, G. J. Snyder, H. Wu and L.-D. Zhao, *J. Am. Chem. Soc.*, 2020, **142**, 4051–4060.
14 M. Samanta and K. Biswas, *J. Am. Chem. Soc.*, 2017, **139**, 9382–9391.
15 H. Wu, C. Chang, D. Feng, Y. Xiao, X. Zhang, Y. Pei, L. Zheng, D. Wu, S. Gong, Y. Chen, J. He, M. G. Kanatzidis and L.-D. Zhao, *Energy Environ. Sci.*, 2015, **8**, 3298–3312.
16 J.-S. Liang, X.-L. Shi, Y. Peng, W.-D. Liu, H.-Q. Yang, C.-Y. Liu, J.-L. Chen, Q. Zhou, L. Miao and Z.-G. Chen, *Adv. Energy Mater.*, 2022, **12**, 2201086.
17 Y. Luo, S. Cai, X. Hua, H. Chen, Q. Liang, C. Du, Y. Zheng, J. Shen, J. Xu, C. Wolverton, V. P. Dravid, Q. Yan and M. G. Kanatzidis, *Adv. Energy Mater.*, 2019, **9**, 1803072.
18 Z. Liu, J. Sun, J. Mao, H. Zhu, W. Ren, J. Zhou, Z. Wang, D. J. Singh, J. Sui, C.-W. Chu and Z. Ren, *Proc. Natl. Acad. Sci. U. S. A.*, 2018, **115**, 5332–5337.
19 Y. Zheng, Q. Zhang, X. Su, H. Xie, S. Shu, T. Chen, G. Tan, Y. Yan, X. Tang, C. Uher and G. J. Snyder, *Adv. Energy Mater.*, 2015, **5**, 1401391.
20 M. Y. Toriyama and G. J. Snyder, *Mater. Horiz.*, 2024, **11**, 1188–1198.
21 L. Müchler, F. Casper, B. Yan, S. Chadov and C. Felser, *Phys. Status Solidi RRL*, 2013, **7**, 91–100.
22 D. Baldomir and D. Faílde, *Sci. Rep.*, 2019, **9**, 6324.

23 N. Xu, Y. Xu and J. Zhu, *npj Quantum Mater.*, 2017, **2**, 51.
24 Y. L. Chen, J. G. Analytis, J.-H. Chu, Z. K. Liu, S.-K. Mo, X. L. Qi, H. J. Zhang, D. H. Lu, X. Dai, Z. Fang, S. C. Zhang, I. R. Fisher, Z. Hussain and Z.-X. Shen, *Science*, 2009, **325**, 178–181.
25 D. Hsieh, Y. Xia, D. Qian, L. Wray, F. Meier, J. H. Dil, J. Osterwalder, L. Patthey, A. V Fedorov, H. Lin, A. Bansil, D. Grauer, Y. S. Hor, R. J. Cava and M. Z. Hasan, *Phys. Rev. Lett.*, 2009, **103**, 146401.
26 H. Zhang, C.-X. Liu, X.-L. Qi, X. Dai, Z. Fang and S.-C. Zhang, *Nat. Phys.*, 2009, **5**, 438–442.
27 Y. Lu, Y. Zhou, W. Wang, M. Hu, X. Huang, D. Mao, S. Huang, L. Xie, P. Lin, B. Jiang, B. Zhu, J. Feng, J. Shi, Q. Lou, Y. Huang, J. Yang, J. Li, G. Li and J. He, *Nat. Nanotechnol.*, 2023, **18**, 1281–1288.
28 Z.-H. Zheng, X.-L. Shi, D.-W. Ao, W.-D. Liu, M. Li, L.-Z. Kou, Y.-X. Chen, F. Li, M. Wei, G.-X. Liang, P. Fan, G. Q. (Max) Lu and Z.-G. Chen, *Nat. Sustain.*, 2023, **6**, 180–191.
29 P. Ghaemi, R. S. K. Mong and J. E. Moore, *Phys. Rev. Lett.*, 2010, **105**, 166603.
30 T. H. Hsieh, H. Lin, J. Liu, W. Duan, A. Bansil and L. Fu, *Nat. Commun.*, 2012, **3**, 982.
31 K. Dybko, M. Szot, A. Szczerbakow, M. U. Gutowska, T. Zajarniuk, J. Z. Domagala, A. Szewczyk, T. Story and W. Zawadzki, *Phys. Rev. B*, 2017, **96**, 205129.
32 M. Zhou, Z. M. Gibbs, H. Wang, Y. Han, C. Xin, L. Li and G. J. Snyder, *Phys. Chem. Chem. Phys.*, 2014, **16**, 20741–20748.
33 S. Misra, B. Wiendlocha, J. Tobola, F. Fesquet, A. Dauscher, B. Lenoir and C. Candolfi, *J. Mater. Chem. C*, 2020, **8**, 977–988.
34 S. Misra, B. Wiendlocha, J. Tobola, F. Fesquet, A. Dauscher, B. Lenoir and C. Candolfi, *J. Mater. Chem. C*, 2020, **8**, 977–988.
35 K. R. Knox, E. S. Bozin, C. D. Malliakas, M. G. Kanatzidis and S. J. L. Billinge, *Phys. Rev. B:Condens. Matter Mater. Phys.*, 2014, **89**, 14102.
36 Z. M. Gibbs, A. LaLonde and G. J. Snyder, *New J. Phys.*, 2013, **15**, 075020.
37 B. Jia, D. Wu, L. Xie, W. Wang, T. Yu, S. Li, Y. Wang, Y. Xu, B. Jiang, Z. Chen, Y. Weng and J. He, *Science*, 2024, **384**, 81–86.
38 A. Banik, U. S. Shenoy, S. Saha, U. V Waghmare and K. Biswas, *J. Am. Chem. Soc.*, 2016, **138**, 13068–13075.
39 L. Zhao, J. Wang, J. Li, J. Liu, C. Wang, J. Wang and X. Wang, *Phys. Chem. Chem. Phys.*, 2019, **21**, 17978–17984.
40 F. Li, X. Liu, S.-R. Li, X.-F. Zhang, N. Ma, X.-J. Li, X.-Y. Lin, L. Chen, H. Wu and L.-M. Wu, *Energy Environ. Sci.*, 2024, **17**, 158–172.
41 Y. Liu, X. Zhang, P. Nan, B. Zou, Q. Zhang, Y. Hou, S. Li, Y. Gong, Q. Liu, B. Ge, O. Cojocaru-Mirédin, Y. Yu, Y. Zhang, G. Chen, M. Wuttig and G. Tang, *Adv. Funct. Mater.*, 2022, **32**, 2209980.
42 A. Banik, B. Vishal, S. Perumal, R. Datta and K. Biswas, *Energy Environ. Sci.*, 2016, **9**, 2011–2019.
43 G. Tan, F. Shi, J. W. Doak, H. Sun, L.-D. Zhao, P. Wang, C. Uher, C. Wolverton, V. P. Dravid and M. G. Kanatzidis, *Energy Environ. Sci.*, 2015, **8**, 267–277.
44 A. Banik, U. S. Shenoy, S. Anand, U. V Waghmare and K. Biswas, *Chem. Mater.*, 2015, **27**, 581–587.
45 U. S. Shenoy and D. K. Bhat, *J. Mater. Chem. C*, 2020, **8**, 2036–2042.
46 G. Tan, F. Shi, S. Hao, H. Chi, L.-D. Zhao, C. Uher, C. Wolverton, V. P. Dravid and M. G. Kanatzidis, *J. Am. Chem. Soc.*, 2015, **137**, 5100–5112.
47 R. Pathak, D. Sarkar and K. Biswas, *Angew. Chem., Int. Ed.*, 2021, **60**, 17686–17692.
48 Y. Kawami, X. Q. Tran, T. Yamamoto, S. Yoshioka, Y. Murakami, S. Matsumura, K. Nogita and J. Zou, *Adv. Mater.*, 2024, 2410508.
49 C. Nie, C. Wang, Y. Xu, Y. Liu, X. Niu, S. Li, Y. Gong, Y. Hou, X. Zhang, D. Zhang, D. Li, Y. Zhang and G. Tang, *Small*, 2023, **19**, 2301298.
50 L. Wang, S. Chang, S. Zheng, T. Fang, W. Cui, P. Bai, L. Yue and Z.-G. Chen, *ACS Appl. Mater. Interfaces*, 2017, **9**, 22612–22619.
51 Z. Ma, J. Lei, D. Zhang, C. Wang, J. Wang, Z. Cheng and Y. Wang, *ACS Appl. Mater. Interfaces*, 2019, **11**, 33792–33802.
52 L. Aggarwal, A. Banik, S. Anand, U. V Waghmare, K. Biswas and G. Sheet, *J. Mater.*, 2016, **2**, 196–202.
53 K. V Mitrofanov, A. V Kolobov, P. Fons, M. Krbal, T. Shintani, J. Tominaga and T. Uruga, *Phys. Rev. B*, 2014, **90**, 134101.
54 C. W. Li, O. Hellman, J. Ma, A. F. May, H. B. Cao, X. Chen, A. D. Christianson, G. Ehlers, D. J. Singh, B. C. Sales and O. Delaire, *Phys. Rev. Lett.*, 2014, **112**, 175501.
55 M. Iizumi, Y. Hamaguchi, K. F. Komatsubara and Y. Kato, *J. Phys. Soc. Jpn.*, 1975, **38**, 443–449.
56 D. Shoenberg, *Magnetic Oscillations in Metals*, Cambridge University Press, 1984.
57 G. J. Snyder, A. Pereyra and R. Gurunathan, *Adv. Funct. Mater.*, 2022, **32**, 2112772.
58 K. H. Lee, S. Kim, J.-C. Lim, J. Y. Cho, H. Yang and H.-S. Kim, *Adv. Funct. Mater.*, 2022, **32**, 2203852.
59 X. Zhang, Z. Chen, S. Lin, B. Zhou, B. Gao and Y. Pei, *ACS Energy Lett.*, 2017, **2**, 2470–2477.
60 L. Wang, M. Hong, Q. Sun, Y. Wang, L. Yue, S. Zheng, J. Zou and Z.-G. Chen, *ACS Appl. Mater. Interfaces*, 2020, **12**, 36370–36379.
61 J. Callaway and H. C. von Baeyer, *Phys. Rev.*, 1960, **120**, 1149–1154.
62 J. Callaway, *Phys. Rev.*, 1959, **113**, 1046–1051.
63 I. K. Dimitrov, M. E. Manley, S. M. Shapiro, J. Yang, W. Zhang, L. D. Chen, Q. Jie, G. Ehlers, A. Podlesnyak, J. Camacho and Q. Li, *Phys. Rev. B*, 2010, **82**, 174301.
64 B. Yang, S. Li, X. Li, Z. Liu, D. Li, H. Zhong and S. Feng, *Intermetallics*, 2021, **136**, 107257.
65 G. Tan, L.-D. Zhao, F. Shi, J. W. Doak, S.-H. Lo, H. Sun, C. Wolverton, V. P. Dravid, C. Uher and M. G. Kanatzidis, *J. Am. Chem. Soc.*, 2014, **136**, 7006–7017.
66 S. Hikami, A. I. Larkin and Y. Nagaoka, *Prog. Theor. Phys.*, 1980, **63**, 707–710.
67 W. Niu, M. Gao, X. Wang, F. Song, J. Du, X. Wang, Y. Xu and R. Zhang, *Sci. Rep.*, 2016, **6**, 26081.

